Direct Observation of Conductive Filaments from 3D Views in Memristive Devices Based on Multilayered SiO_2: Formation, Dissolution, and Vaporization

Bo Zhang[a], Bin Gu[a], Janicek Petr[b,c], Jhonatan Rodriguez-Pereira[c], Stanislav Slang[c], Tomas Wagner[c,d*]*

[a]College of Physics, Hebei Normal University, Shijiazhuang 050024, China

[b]Institute of Applied Physics and Mathematics, Faculty of Chemical Technology, University of Pardubice, Studentska 95, Pardubice 530 02, Czech Republic

[c]Center of Materials and Nanotechnologies, Faculty of Chemical Technology, University of Pardubice, nam. Cs. Legii 565, Pardubice 530 02, Czech Republic

[d]Department of General and Inorganic Chemistry, Faculty of Chemical Technology, University of Pardubice, Studentska 573, 532 10 Pardubice, Czech Republic

KEYWORDS conductive filament; memristive device; resistive switching; ReRAM；

electrochemical metallization memory

ABSTRACT Memristive devices, also known as memristors or ReRAMs, are promising candidates for accessing next-generation memory. In classic electrochemical metallization (ECM) theory, there are only two states of conductive filaments: formation and dissolution. In our experiment, we found that the metallic filaments also vaporized, leaving observable defects in a series of memristive devices based on a Cu-doped multilayered SiO_2 electrolyte layer. Furthermore, the vapour from conductive filaments exfoliated adjacent single layers of multilayered SiO_2. The morphologies of the conductive filaments in a memristive device (W/Cu-doped SiO_2/Ag) were studied using an SEM (scanning electron microscope) instrument equipped with an FIB (focused ion beam) module. With the gradual removal of the electrolyte layer, cross-sectional images of the conductive filaments were captured from perspective, top and side views.

Based on these images, a three-dimensional model of the conductive filaments was proposed. All the findings suggested that the SET and RESET processes were complex and involved the simultaneous formation, dissolution and vaporization of conductive filaments. The vaporization of the conductive filaments permanently changed the surface morphology of the devices. This model, presented at the end of our paper, explains the irregular phenomena that occurred in I-V measurements.

INTRODUCTION

The ECM (electrochemical metallization model) interprets the mechanism of resistive switching with metal-doped chalcogenides (such as Ag_2S, CuS, AgGeSe, and CuGeSe) or oxides (such as WO_3, SiO_2, ZrO_2, Ta_2O_5, and ZnO)[1–12]. Memristive devices have been widely utilized for data storage, computation, synaptic emulation, logic gates, FPGAs, encryption and radiofrequency communication[13–16]. The cyclic changes in the resistance states are accompanied by the formation and dissolution of the metallic filament. Whereas the filament bridges the top and bottom electrodes after the positive DC sweep, the devices exhibit a LRS (low resistance state). In contrast, a negative DC sweep leads to dissolution of the conductive filament, and the memristive device is in the HRS (high resistance state)[17]. Furthermore, the ECM also connects the rupture of conductive filaments with Joule heat. Therefore, the competition between Joule heat and redox reactions has been described in the ECM model. Once the redox reaction dominates, the memristive cell is prone to unipolar switching[18].

Since the discovery of resistive switching behavior, researchers have found various methods for imaging conductive filaments[19–22]. However, direct observation of a conductive filament within a thin film is still difficult[23]. Therefore, the simulation of conductive filaments was often used[24]. In recent years, in situ transmission electron microscopy (TEM) has been widely utilized to demonstrate the morphology of conductive filaments[25]. Nevertheless, observing a sample using in situ TEM requires a complex preparation procedure. Furthermore, observing a 3D model of a conductive filament via TEM imaging is difficult.

EXPERIMENTAL METHODS

The devices were prepared using RF sputtering. This led to the deposition of multilayered Cu-doped SiO_2 onto the substrate by means of a combination of Cu and SiO_2 targets. The RF sputtering configuration is shown in Figure S1. The composition of the Cu-doped SiO_2 was regulated by the size of the opening of the aperture and the RF power. All coating processes were conducted in a vacuum chamber at a base pressure of $1x10^{-5}$ mbar using argon gas (99.999%) at a flow rate of 30 sccm. Exfoliation of the Cu-doped SiO_2 on the substrate of the silicon wafer was completed using treatment with a saturated $FeCl_3$ acetone solution. Then, the samples were rinsed with distilled water many times and transferred to an optical microscope for observation. The details of the surface morphology were also examined using an SEM S4800 (Hitachi) at an acceleration voltage of 10 kV. The height of the steps and topographical image were studied by means of an AFM (atomic force microscope) (Veeco). X-ray photoelectron spectroscopy (XPS) was conducted using a Thermo Scientific^{TM} K-Alpha spectrometer equipped with a monochromatic Al Kα X-ray source (1486.6 eV) operated at 100 W. The samples were analysed under vacuum ($P < 10^{-8}$ mbar) with a pass energy of 150 eV (survey scans) or 25 eV (high-resolution scans). All the XPS peaks were calibrated for adventitious carbon with a C1s peak binding energy of 284.8 eV. The experimental

XPS peaks were fitted using Avantage software. The crystalline structure of the materials was characterized via X-ray diffraction (XRD) (Rigaku) using Cu Kα radiation (λ=0.1542).

The devices were fabricated on a silica glass substrate in a classic crossbar configuration with 3 layers (W/Cu-doped SiO_2/Ag). The electrodes were deposited via a stencil, where the size of the cross point was 100 μm × 100 μm. Subsequent DC sweeps were measured using a Keithley 2600 multimeter equipped with probes. A series of electrolytes with different thicknesses and Cu concentrations were deposited on silicon substrates, as shown in Table S3. All the devices were measured by a DC sweep until the resistance was stable. After the DC sweep had been measured, all the samples were studied via SEM imaging. The electrical field and heat distribution of the devices were simulated by means of COMSOL software. The corresponding equations, boundary conditions, material properties and geometrical dimensions can be found in the supplementary materials.

Ga ion milling of the sample was carried out using a dual beam scanning electron microscope (DBEM) (Tescan, LYRA3), and FIB was performed at a 30 kV acceleration voltage with an emission current of 2 μA and a beam current of 12 nA. Two types of milling were used: cross-sectional and top milling. The top milling was accompanied by SEM imaging every 5 minutes.

RESULTS AND DISCUSSION

In our experiments, we fabricated a device with a structure of W(BE, bottom electrode)/Cu-doped SiO_2/Ag(TE, top electrode). SiO_2 doped with Cu was synthesized using RF sputtering. The morphology of the conductive filaments was obtained from perspective, top and side views using an SEM instrument equipped with an FIB milling module. The results revealed that there was vaporization of a conductive filament during the SET process. This vaporization was induced by Joule heating. Pores were left on the surface of the memristive device. A similar morphology was also observed in the other devices in which the electrolyte was fabricated with different Cu contents and thicknesses. By means of COMSOL simulation, we employed two methods (decreasing the compliance current and extra cooling of the tungsten electrode) to reduce Joule heating. Thus, we improved the endurance of the memristive device from 100 cycles to 730 cycles.

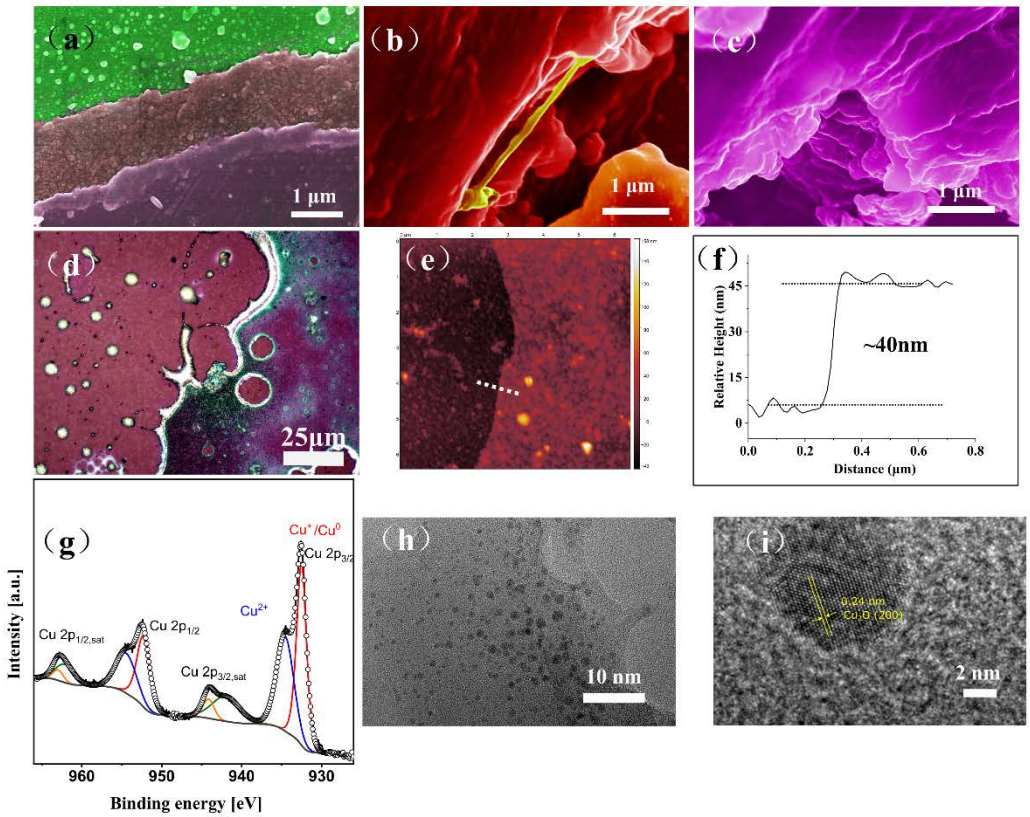

Figure 1. The structure and composition of as-deposited multilayered $Cu_{26}(SiO_2)_{74}$: (a)-(c) steps of single layers taken using SEM; (d) optical image of single layers; (e), (f) topographic images of steps where the profiles of a step in (f) are taken from a dashed line of (e); (g) Cu 2p XPS high resolution spectrum of $Cu_{26}(SiO_2)_{74}$ material; (h), (i) TEM images of multilayered $Cu_{26}(SiO_2)_{74}$ with different resolution scales where the interplanar spacing is marked in (f).

Cu doped into the SiO_2 electrolyte layer was prepared using RF sputtering. Before this, the Cu and SiO_2 targets were vertically positioned in the sputtering chamber. During the deposition process, Cu was sputtered with SiO_2. Since both targets (Cu and SiO_2) in our method were perpendicularlyly aligned with the substrate, oblique deposition was prevented. The Cu

content was regulated by the size of the openings in the aperture and the amount of sputtering energy. A larger opening and lower power of the sputtering energy resulted in a high concentration of elemental Cu, the details of which are shown in Figure S1.

The structure and composition of the $Cu_{26}(SiO_2)_{74}$ electrolyte layer are shown in Figure 1. The as-deposited Cu-doped SiO_2 had a multilayered structure. Pure SiO_2 is normally etched by HF in the electronic industry[26]. When the Cu concentration in our experiment reached the saturation value, Cu began to precipitate at the interfaces of the single layers. Therefore, the Cu-doped SiO_2 was exfoliated using $FeCl_3$ acetone solution. First, the Cu particles reacted with $FeCl_3$, and then the adjacent layers were further delaminated by means of acetone vapour. Moreover, some single layers were dispersed in a saturated $FeCl_3$ acetone solution, leaving a morphology with steps, as shown in Figure 1a. Afterwards, the detailed step-like morphology was observed via SEM (Hitachi, S4800) under a 10 kV accelerating voltage. Figure 1b shows a freestanding single layer (marked in yellow) suspended at the edge of other single layers. In the cross-sectional view, more than six single layers can be observed, as shown in Figure 1c. The other samples had similar surface morphologies, as shown in Figure S2. After the etching and exfoliation of the single layers, the appearance of SiO_2 changed under the optical microscope from colorless to red and blue, as shown in Figure 1d. Its mechanism is attributed to the light inference effect [27]. The other samples shown in Figure S3 displayed more complex rainbow colours. Since the multilayered electrolyte layers in our experiment were synthesized by means of sputtering, the size of the free-standing single layers was square millimeters. Therefore, this approach is suitable for the fabrication of electronic devices. Figure 1e,f shows topographic images of $FeCl_3$ etched with multilayered $Cu_{26}(SiO_2)_{74}$, which were measured via AFM (Multimode, Veeco). The thickness of the free-

standing single layer was approximately 40 nm. In the other samples, we could observe that the minimum thickness of a free-standing single layer was ~3 nm, while the maximum thickness was ~45 nm, as shown in Figure S4.

The composition of the Cu-doped SiO_2 was studied using XPS and XRD, the results of which are shown in Figures S5-S7. The crystalline structure of the materials was first characterized via X-ray diffraction (XRD) (Rigaku) using Cu Kα radiation (λ=0.1542 nm). Based on the XRD patterns (Figure S7), the structure of SiO_2 was amorphous. We believe that this type of multilayered structure is formed during self-assembly. X-ray photoelectron spectroscopy (XPS) was conducted using a Thermo Scientific^{TM} K-Alpha spectrometer equipped with a monochromatic Al Kα X-ray source (1486.6 eV) operated at 100 W. The samples were analysed under vacuum ($P < 10^{-8}$ mbar) with a pass energy of 150 eV (survey scans) or 25 eV (high-resolution scans). All the XPS peaks were calibrated for adventitious carbon with a C1s peak binding energy of 284.8 eV. Since the binding energies of Cu and Cu^+ were close to 933 eV, they could not be clearly distinguished. The presence of Cu^{2+} on the surface was also detected, corresponding to the peak at 935 eV. The XRD patterns further confirmed that the Cu-doped multilayered SiO_2 consisted of two common components (Cu_2O and Cu), where the XRD peak centred at 36.3° signified the Cu_2O reflection [28]. The atomic concentrations of the studied layers were calculated by means of quantitative analysis of the Cu 2p and Si 2p peaks.

The structure of the free-standing single layers was further studied using TEM (FEIF F20). First, Cu-doped SiO_2 was deposited on the NaCl substrate. Then, the free-standing flakes were dispersed

into the solution and transferred to a Cu grid for TEM imaging. Figures 1h and S8 exhibit the morphology of single layers with dark dots, which consisted of crystalline Cu_2O under high magnification. The lattice spacing was 0.24 nm, which corresponded with the (2 2 0) crystal planes of Cu_2O. A similar morphology of dark dots has also been reported in the literature. This suggests that Cu_2O crystallites are embedded in the SiO_2 matrix[29].

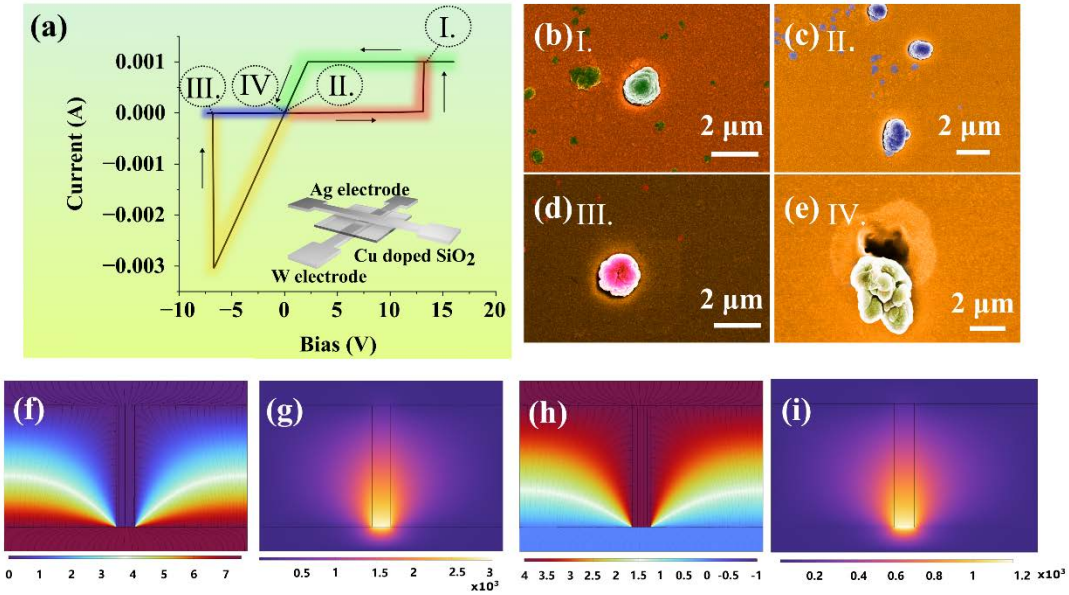

Figure 2. (a) The I-V characteristics of the W(BE)/Cu-doped SiO_2 [$Cu_{26}(SiO_2)_{74}$]/Ag(TE) device where the insert shows its structure. The I-V curve is divided into four different stages (marked by colours and arrows). The SEM images were taken at the end of each stage (marked from I to IV); (b)-(e) development of the surface morphology based on the markers in (a); (f) and (h) the electric

field (scale below in volts); and (g) (i) the temperature distribution (scale below in degrees Celsius) of the W(BE)/Cu-doped SiO_2 [$Cu_{11}(SiO_2)_{89}$]/Ag(TE) device at -7.5 V (f), (g) and 4 V (h), (i).

The cross-sectional view of filaments has widely been studied by means of in situ TEM [29]. However, there is still a lack of direct observation of a 3D view of a conductive filament. In our experiments, the memristive cell was fabricated in a crossbar configuration where the area of the cross-point was 100 μm × 100 μm. I-V measurements were taken with a Keithley instrument equipped with tungsten probes, in which the positive probe contacted the top Ag electrode and the negative electrode contacted the bottom W electrode. Since the electrolyte layer length reached 1 μm, our prior test suggested that the memristive device with the Cu electrode had an ultrahigh SET threshold. Therefore, Ag was selected as the active electrode for a lower SET threshold.

A Ag or Cu-doped SiO_2 electrolyte layer is a common material for memristive cells [30–33]. In our case, during the positive DC sweep, the Cu nanoparticles embedded inside the electrolyte layer and bottom Ag electrode were oxidized. Consequently, Cu ions with small amounts of Ag ions migrated toward the topmost tungsten electrode and were reduced into conductive filaments. Nevertheless, since the SiO_2 electrolyte layer was heavily doped with Cu before DC sweeping, the conductive filament mainly consisted of Cu. Once the conductive filament bridged the metal electrodes, the current increased to the compliance current. In the negative DC sweep, the conductive filament was oxidized, and Ag or Cu ions were reduced in the vicinity of the bottom tungsten electrode, while the resistance of the overall memristive device increased.

First, a DC sweep was applied to a W(BE)/$Cu_{26}(SiO_2)_{74}$/Ag(TE) memristive device utilizing a range of 16 V to -7.3 V with 1 mA current compliance. The I-V curve was divided into four stages.

After each stage, the surface morphology of the electrode was imaged using SEM (Hitachi, S4800) at a 10 kV accelerating voltage. At point I (red, as shown in Figure 2a), a filament was created during the SET process, and the current reached the compliance value (1 mA). Compared to the other devices described in the literature, the SET threshold of ~14 V was clearly greater in devices with a 1 μm thick electrolyte layer[22]. Figure 2b shows the surface morphology at point I of the I-V curve (Figure 2a). The original SEM images, which are attached as supplementary material, were processed with colours. (Figure S9). As shown in Figure 2c, the morphology of the particles was similar to that in Figure 2b, whereas the bias decreased to 0 V at point II. We continued decreasing the bias until it reached -6.7 V. Then, the device was switched to HRS, in which the filament was dissolved at point III. The morphology of the particles remained similar, as shown in Figure 2d. Figure 2e was captured at point IV when the overall DC sweep was completed. The particle shifted to one side of the underlying pore. The creation of particles was observed in one of our previous experiments on Ag-doped As_2S_3 devices where Ag particles were deposited on the surface of the device during the SET process and disappeared during the RESET process[31]. Since the defects in the pores and particles permanently changed the electrolyte, the formation of conductive filaments was attributed to the hard breakdown induced by Joule heating. Therefore, the thermal and electric field distributions of the conductive filament were simulated using COMSOL software, as shown in Figures (2f-i), and other details can be found in S10- S12 and the text around the supplementary materials. When the Cu particles precipitated inside the silicon oxide, the simulation suggested that the electric field was more concentrated, which assisted in the growth of a conductive filament (Figure S10). Since the experiment was performed in an ambient environment, the SET threshold can be partially influenced by moisture, which improves the conductivity of the electrolyte layer and modulates the switching kinetics. The parameters of the

material used in this simulation are listed in Table S1 and Figure S9 (e)-(f). A description of the model/governing equations is also presented in the supplementary material (Table S2, Figures S10-S12 and related text). In the multiphysics simulation, an electric field with heat transfer from the Poole–Frenkel–Schottky dependence model was used for additional tungsten oxide (thickness of 1 nm) inserted between the tungsten (BE) and electrolyte layers. In the simulation without the tungsten oxide layer, the maximum temperature reached an unreasonably high level (Figure S11). As a result, the overall current and bias did not correspond with the I-V curve (Figure S12). As shown in Figures 2f-i, the column of the Cu conductive filament bridged the electrodes, which led to LRS. Due to the low conductivity of tungsten oxide (2 S/m), a large electric field was concentrated on the tungsten oxide layer, as demonstrated in Figure 2f. Consequently, the maximum temperature on the tungsten oxide layer was higher than the melting point of copper (1085°C). In this case, the copper filament can naturally dissolve into the SiO_2 layer, whereas the particles and the pores were also created during this procedure. Figure 2h,i shows a temperature greater than 1000°C at 4 V, meaning that some parts of the filament were vaporized with breakdown of the material. Since the experiment was performed in an ambient environment, the SET threshold can be partially influenced by moisture, which improves the conductivity of the electrolyte layer and contributes to the formation of defects [34].

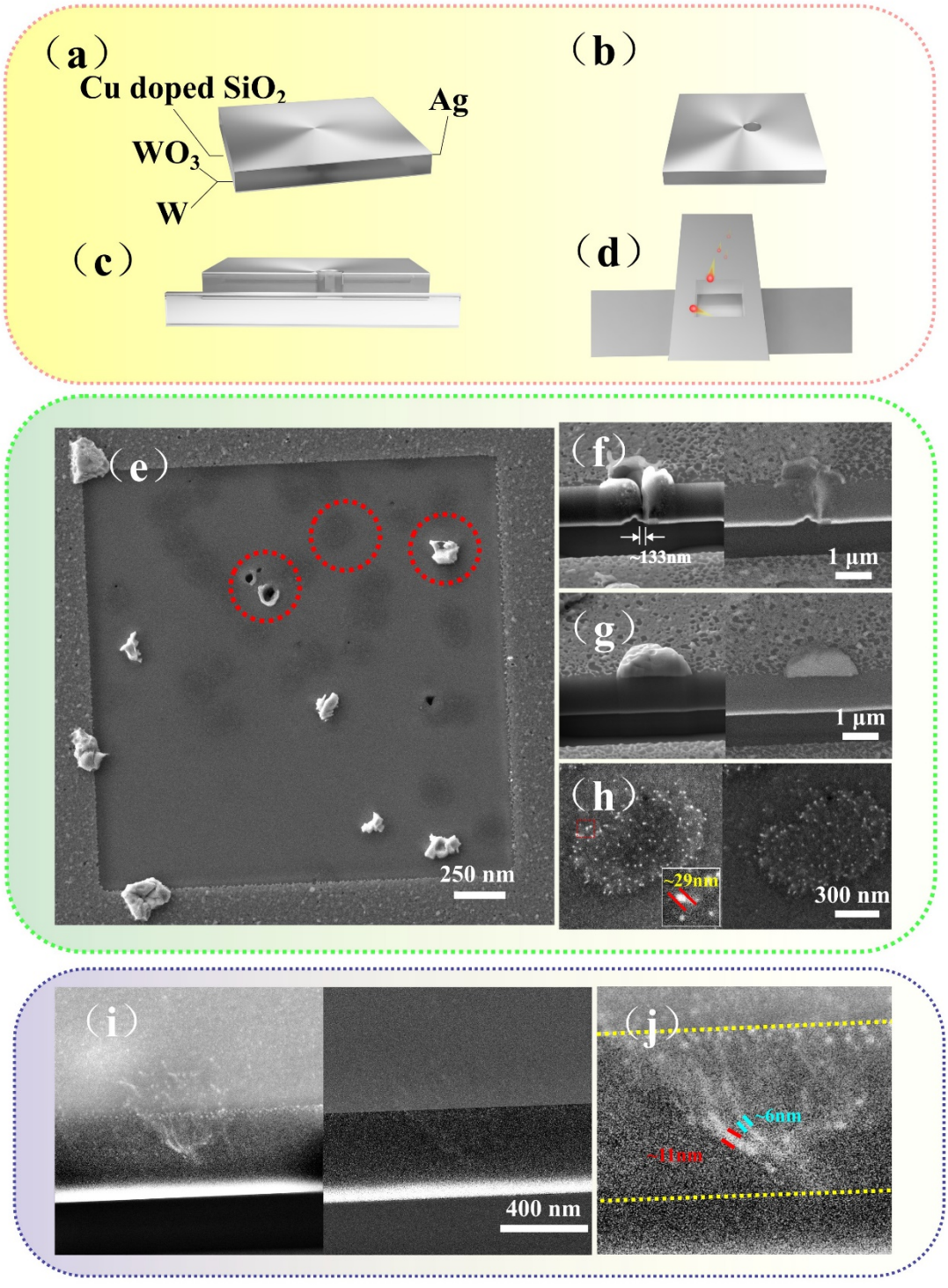
(a)
Cu doped SiO2
Ag
WO3
W
(b)
(c)
(d)
(e)
250 nm
(f)
~133nm
1 μm
(g)
1 μm
(h)
~29nm
300 nm
(i)
400 nm
(j)
~6nm
~11nm

Figure 3. FIB cutting and etching of the W(BE)/Cu-doped SiO_2 [$Cu_{11}(SiO_2)_{89}$]/Ag(TE) device: (a) the illustrative scheme of the memristive device used in I-V measurement where the WO_3 layer was created in proximity to the tungsten layer; (b) the illustrative scheme of the pores; (c) the illustrative scheme of FIB milling and cross-sectional scheme of the pores; (d) the illustrative top-down scheme with a large area of FIB milling; (e) the SEM image of the devices milled for a period of 5 minutes where the most common defects are marked in red; (f) the cross-sectional SEM image of the pores in the secondary electron, left) and backscattered electron, right (SE) modes. The diameter of the filament was ~133 nm. (g) Cross-sectional SEM image of particles in the SE (left) and BSE (right) modes. (h) Cross-sectional SEM image (top view) of the conductive filaments in the SE (left) and BSE (right) modes. The diameter of the branches of the filament was ~29 nm, which is marked in the inset; (i) the cross-sectional (side view) view of the conductive filaments in the SE (left) and BSE (right) modes; (j) the enlarged area from part of i. The boundary of the electrolyte layer is marked by the yellow dashed lines. The diameters of the branches of the conductive filaments were ~6 nm (blue) and ~11 nm (red).

To observe the pores, a memristive device was switched to the LRS after one normal cycle (Figure S13). The structure of the device after I-V measurements is shown in Figure 3a. Two types of device milling, cross-sectional and top milling, were employed in our experiment. A section was prepared along the diameter of each defect (pores and particles), as shown in Figure 3b and c. Afterwards, top-down milling was carried out via SEM equipped with a FIB (Tescan, LYRA3), as schematically demonstrated in Figure 3d. FIB was performed at a 30 kV acceleration voltage with an emission current of 2 μA and a beam current of 12 nA on a large area of the device. As shown in Figure 3e, the device was milled for 5 minutes. Three types of featured morphologies, pores,

white particles, and dark regions, are marked with red circles. The pore was cross-sectionally cut. The diameter of the conductive filament was 133 nm (Figure 3f). The SEM image in the BSE mode showed that it consisted of heavier elements (lighter colours). Furthermore, the pores, which originated from the conductive filaments, suggested that vaporization of the conductive filaments had occurred. Figure S14 (a)-(b) clearly shows an empty pore where all of the filaments were vaporized due to Joule heating.

A cross-sectional view of the particles is presented in Figure 3g. Further EDX analysis (Figure S15) showed that the precipitated particles were copper. Such a phenomenon can also be found in a Cu-doped chalcogenide thin film[35]. As demonstrated in Figure 3h, the SEM image shows the top view of a conductive filament. The conductive filament in Figure 3h also shows branches, which are obviously different from those in Figure 3f. The diameter of the branch, marked by red lines, was approximately 29 nm. The morphology of the conductive filament was also observed from a side view in a cross-sectional image, as shown in Figures 3i,j. The filament branches were approximately 6 nm and 11 nm wide, respectively. The filaments bridged the top and bottom electrodes. The EDS spectrum of conductive filaments suggested that the conductive filament consisted of Cu as shown in Figure S14 (c)-(d). In our opinion, Ag element, whose the concentration might be too low, was not detected.

After milling from the FIB, the formation of conductive filaments was observed. In the SET process, filaments grew under a positive DC sweep. Once the filaments bridged the top and bottom electrodes, the device was switched to LRS, which simultaneously produced a large amount of

Joule heat. Subsequently, some filaments dissolved into the SiO_2 electrolyte layer, while others merged into a thick filament. The thick filaments could not completely dissolve into the electrolyte layer, and some parts vaporized due to an increased bias. As a result, the vapour broke the surrounding thick filament in the electrolyte layer in the vicinity of the tungsten electrode, which left a pore throughout the electrolyte layer.

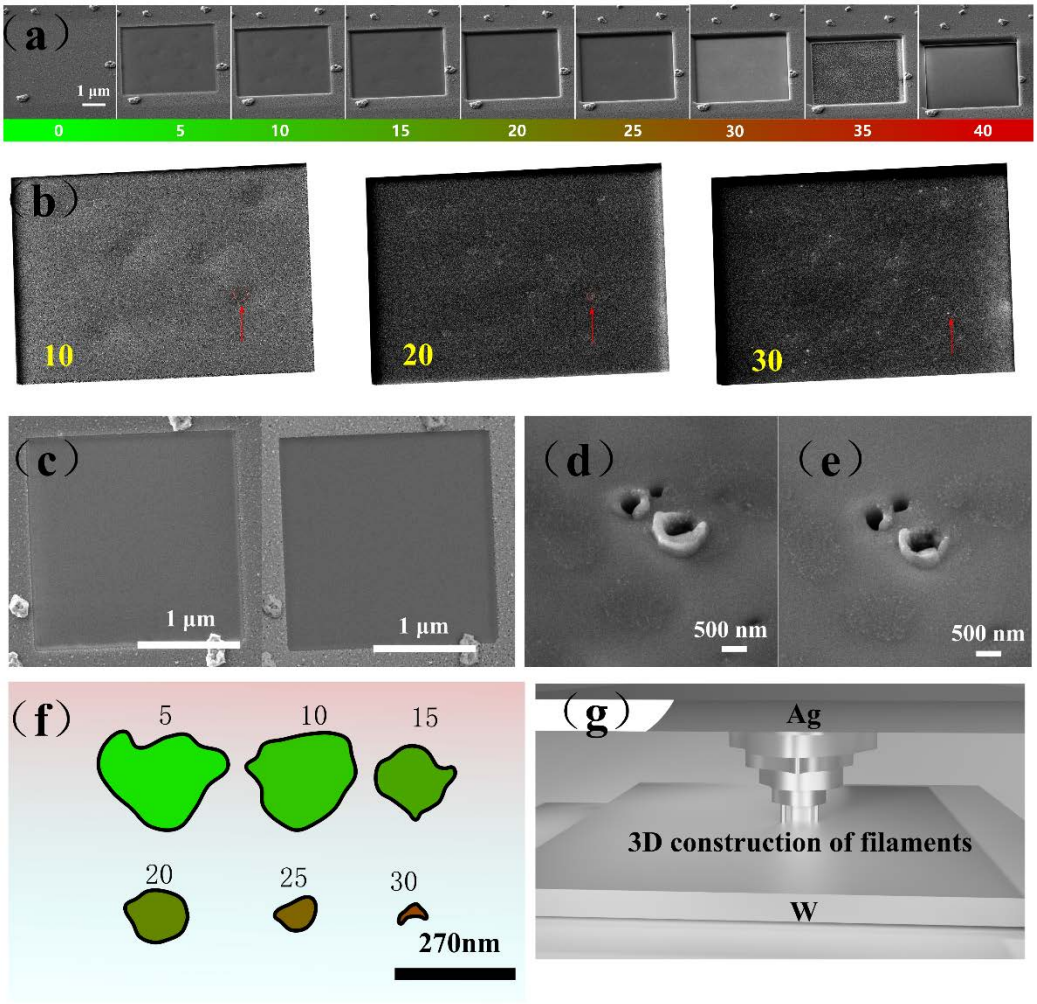

Figure 4. FIB cutting and construction of 3D conductive filaments: (a) SEM images taken every 5 minutes during the milling of the device. The time (in minutes) is marked under the images; (b) the enlarged images taken from part of (a) and the size variation of the conductive filament is

marked by the red arrows and the outlined squares; (c) the etching of the device in the region outside the electrode in SE (left) and BSE (right) modes where no conductive filament was present; (d) the pore after 5 minutes of milling; (e) the pore taken from (d) after another 5 minutes of milling; (f) the outlines of the conductive filaments obtained from (a) where the time of milling is marked above the outlines; (g) the 3D reconstruction of the conductive filament based on (f).

TEM imaging is restricted by many factors, e.g., it only provides a multilayered view of conductive filaments[37]. In our experiment, we applied a new method to characterize the morphology of conductive filaments using FIB milling. The surface of the region for ion milling should be free of surface Cu particles, as the Cu particles, which cover the underlying electrolyte, slow the ion milling process (as shown in Figure S16). Once top-down ion milling started, SEM images were taken every 5 minutes. Figure 4a shows the surface morphology with elapsed time. The surface was evenly removed during milling. Figure 4b shows enlarged images of Figure 4a during milling for 10, 20 and 30 minutes. When the milling continued, the conductive filaments marked with a red arrow shrank. A conductive filament, similar to that in Figure 3h, was found only at the cross-point of the electrodes, as shown in Figure 4c. Nevertheless, the pores are not suitable for top-down FIB milling. As shown in Figures 4d and e, milling for a long duration could remove the extra material from the boundary of the pores and increase their size.

A 3D model of a conductive filament can be obtained based on the SEM images. First, in our experiment, cross-sections of the conductive filaments were plotted from each SEM image, as shown in Figure 4f. Then, the conductive filaments were vertically aligned to the surface of the

electrodes and further processed with 3D modelling software. The result is demonstrated in Figure 4g. The conductive filament has a cone shape, which corresponds with that shown in Figure 3i. The 3D model can further be improved using a shorter interval of modelling and better resolution of SEM imaging. However, as shown in Figure 3a, a slow drift of the sample had a severe impact on the SEM image. Therefore, tracking and imaging of a filament are still difficult over a longer period of time.

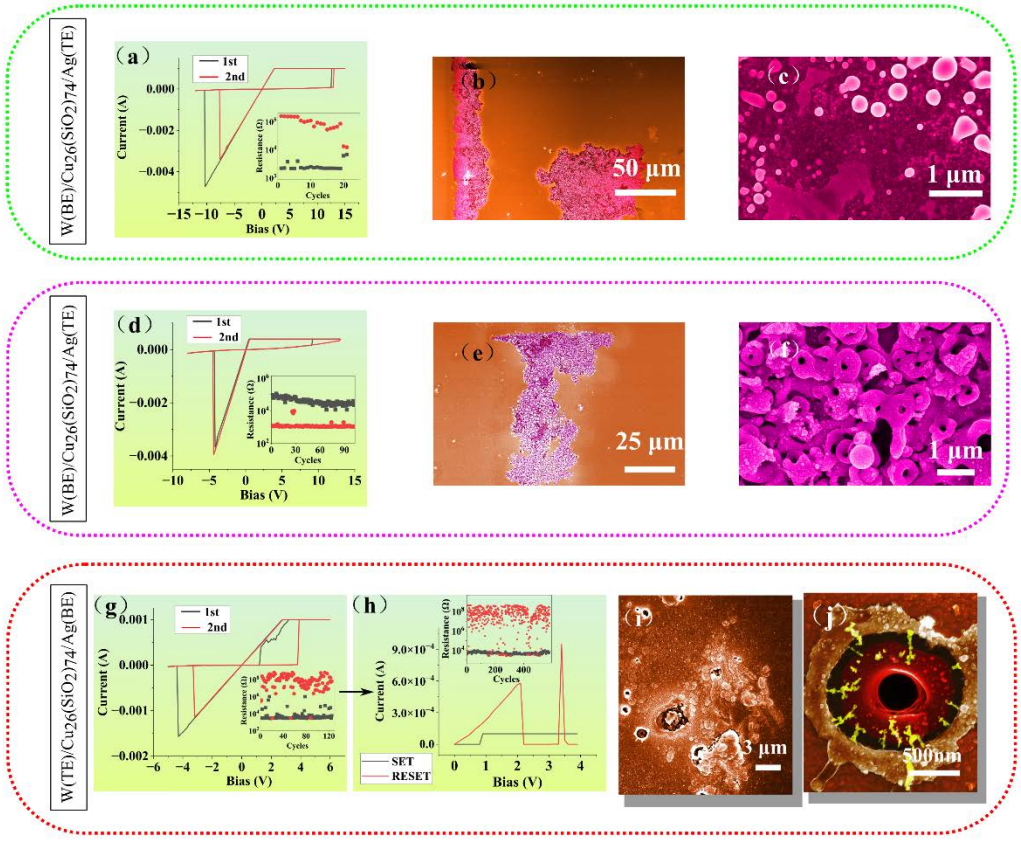

Figure 5. Endurance of the memristive device: (a) I-V curve of the W(BE)/Cu-doped SiO_2 $[Cu_{11}(SiO_2)_{89}]$/Ag(TE) memristive device with a 1 mA compliance current; inset shows the endurance property of the device; (b), (c) the surface morphology of the W(BE)/Cu-doped SiO_2 $[Cu_{11}(SiO_2)_{89}]$/Ag(TE) memritive device after failure; (d) I-V curve of the W(BE)/Cu-doped SiO_2 $[Cu_{11}(SiO_2)_{89}]$/Ag(TE) memristive device with a 0.1 mA compliance current. The inset shows the endurance property of the device; (e), (f) the surface morphology of the W(BE)/Cu-doped SiO_2 $[Cu_{11}(SiO_2)_{89}]$/Ag(TE) memristive device after failure; (g) the bipolar switching behavior of the W(TE)/Cu-doped SiO_2 $[Cu_{11}(SiO_2)_{89}]$/Ag(BE) memristive device; the inset shows the endurance of the device; (h) the unipolar switching behavior of the W(TE)/Cu-doped SiO_2 $[Cu_{11}(SiO_2)_{89}]$/Ag(BE) memristive device. The inset shows the endurance of the device; (i), (j) the pores and the conductive filament (marked with yellow) of the W(TE)/Cu-doped SiO_2 $[Cu_{11}(SiO_2)_{89}]$/Ag(BE) memritive device after failure.

As demonstrated in Figure 5, two different algorithms were used to explore the endurance of the (W(TE)/Cu-doped SiO_2 $[Cu_{11}(SiO_2)_{89}]$/Ag(BE) memristive devices, and the endurance was achieved according to the literature[36]. The I-V measurements were performed until the resistance of the devices remained unchanged and no LRS or HRS could be achieved. This was manifested as a permanent breakdown of the device[37]. We designed 3 types of memritive devices to explore the influence of Joule heat, where the measurement setup in Figure 5a corresponds with that of Figures 2 and 3. The device was continuously operated for 20 cycles under a 1 mA compliance current, and the endurance is presented in Figure S17. The SEM images in Figures 5b and 5c were taken after the I-V test was performed. The defects, for example, pores and bubbles, are marked in pink. These voids were the result of vaporization of the conductive

filament, which delaminated the adjacent single layers. A similar morphology has also been reported in Pt/TiO_2/Pt memristive devices. The bubbles can migrate and disappear under different biases[38]. Therefore, defects are also created in VCM (valance change mechanism) memristive devices. The permanent failure of the Cu/ZnO:Mn/Pt device is attributed to Joule heat, and a lower compliance current is suggested for this device than for the other devices[39]. In our experiment, to achieve more cycles, we decreased the compliance current from 1 mA to 0.1 mA. More than 100 cycles were obtained, as shown in Figure 5d. The simulation of the thermal distribution in Figure 2 demonstrates that the heat concentration in the tungsten oxide layer decreased the endurance of the device. After 100 cycles, the defects (as shown in Figures 5e,f) were mainly pores, and the overall size of the defects (purple) was comparable to that in Figure 4d. In our opinion, the creation of the pores was associated with a bubble burst.

To increase heat dissipation, we used a tungsten electrode as the top electrode for better cooling. The I-V curves in Figures 5g and h show more than 730 cycles in total, which included 130 bipolar cycles and 600 unipolar cycles, respectively. The transition between bipolar and unipolar resistive switching was caused by Cu precipitation. At the beginning of the DC sweep, Cu particles were gradually deposited beneath the tungsten electrode. The top electrode was changed from inert to active. As a result, the Joule heat of the top electrode was greatly reduced. There was only a small region with defects (Figure 5i) in comparison with the previous two cases (Figure 5b, e). Moreover, horizonal growth of the conductive filaments was also found around the pores, which were first created between two adjacent single layers. The filament consisted of nanosized Cu particles (marked in yellow), as presented in the enlarged image in Figure 5j.

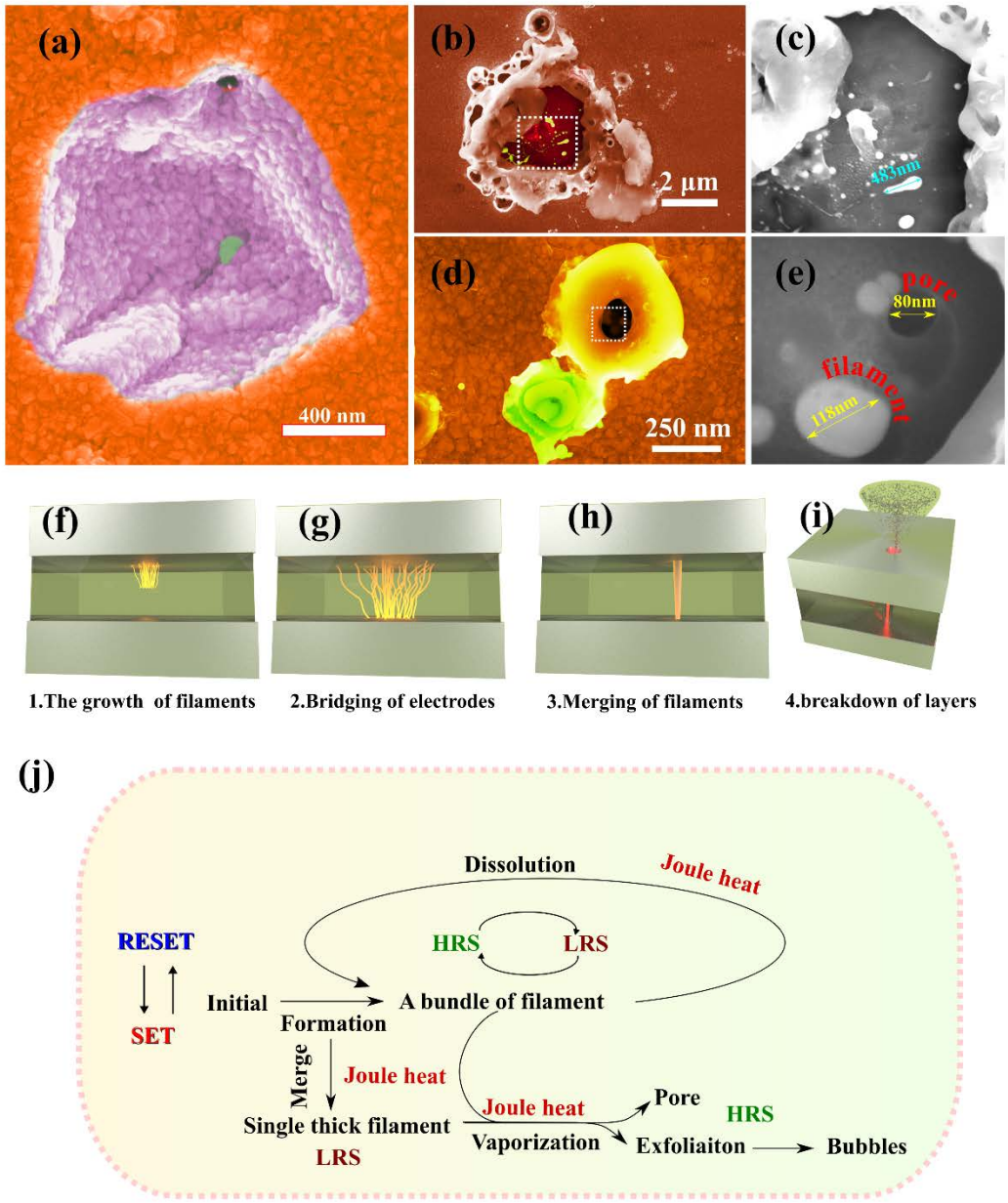

Figure 6. (a) The surface morphology of the W(BE)/multilayered $Cu_{0.6}(SiO_2)_{99.4}$(500 nm)/Ag(TE) device after 20 cycles where a defect in the pore was observed; (b), (c) the surface morphology of the W(BE)/multilayered $Cu_5(SiO_2)_{95}$(500 nm)/Ag(TE) device after 800 cycles where the anisotropic conductive filament with a diameter of 483 nm, (c) is demonstrated from the enlarged

image of (b) (the outlined square); (d), (e) the coexistence of the pores and filaments in the W(BE)/multilayered $Cu_5(SiO_2)_{95}$ (500 nm)/Ag(TE) device where the pores and conductive filaments were observed in a pore enlarged from (d); (f)- (h) the demonstration of filament growth with four different stages; (j) the flow charts regarding the mechanism of filament growth.

Figures 1-4 mainly focus on the memristive device with the $Cu_{26}(SiO_2)_{74}$ electrolyte (1000 nm thick). We also fabricated a series of memristive devices with electrolytes of different Cu concentrations and thicknesses. The performance and surface morphology of the materials after I-V measurements are listed in Table S3 and shown in Figures S17-S30. All the devices were measured with a DC sweep until failure occurred. Under the same external bias, a thinner electrolyte layer resulted in a stronger electric field and hence a thicker filament. For instance, in a device with SiO_2 and a $Cu_{0.6}(SiO_2)_{99.4}$ electrolyte (33 nm thick), the device could not be switched back to a HRS at -20 V. With high Cu concentrations, the embedded Cu nanosized particles and ion migration maintained the device at a constant LRS. An external bias led to an increased concentration of Ag ions in the devices with thinner electrolytes. The corresponding SEM images in Figure S21 exhibit dissolution of the top Ag electrode. The excess ions further resulted in uncontrollable growth of the filament. Moreover, some devices showed a morphology of bubbles. The maximum size of the bubbles reached 5 μm in the devices with thinner electrolytes (as shown in Figures S19-20). The SET threshold decreased with increasing number of cycles, as demonstrated in Figure S30. When the electrolyte layer was 1000 micrometres thick, suitable concentrations of Cu ions were necessary for the formation of filaments. For example, the SiO_2, $Cu_{0.6}(SiO_2)_{99.4}$ memristive device and $Cu(SiO_2)_{95}$ electrolyte layers with a thickness of 1000 nm did not exhibit any formation of the conductive filament until the bias reached 20 V. The

compositions of an electrolyte layer with a suitable Cu concentration and correct thickness are diagonally circled in Table S3, where the device with the $Cu_5(SiO_2)_{95}$ electrolyte layer has the best performance of all the memristive devices.

For devices with a smaller thickness, the sizes of the defects were greater. Figure 6a shows a pore created in the W(BE)/$Cu_{0.6}(SiO_2)_{99.4}$ (500 nm)/Ag(TE) device. The vaporization of the conductive filament left a cone-shaped pore. This was similar to the cross-sectional SEM image in Figure 3j. The bottom electrode is marked in green. The sidewall of the pore was smooth. However, in some other cases, the vaporization exfoliated the single layers, as shown in Figures 6b,c. A cross-sectional image of the filaments from the top view is shown at the bottom of the pore, as shown in Figure 6b. The shape of the filaments is anisotropic. Figures 6d and e demonstrate the coexistence of the filament and pore at one place. They also showed that the filament in the pore was vaporized, which resulted in the formation of another giant pore.

The relationships among the filament, vaporization, and single layers are demonstrated in Figures 2-6. We believe that the SET or RESET process should not be simple and involve only the formation or dissolution of filaments. In other words, the formation and dissolution of filaments occurred simultaneously during the SET and RESET processes. They were in dynamic competition. Therefore, unstable resistance states appeared during a DC sweep, as shown in Figure S30. The filament was created in the SET process, whereas the bias exceeded the threshold. When the filaments bridged the top and bottom electrodes, the current dramatically increased. As a result, substantial Joule heat was created, as demonstrated in Figures 6f,g. Then, the newly formed

conductive filaments with branches were thermally dissolved. Such competition between formation and dissolution could occur many times, ultimately resulting in the formation of a thick filament, as shown in Figure 6h. According to the I-V curve, the current initially fluctuated between the LRS and HRS during the SET process and then stabilized during the LRS. This process permanently changed the morphology of the memristive device, which is confirmed in Figures S18-S31. Figure S18 shows the region of the stable filament, which is marked with a red circle. The lighter surrounding area is shown in the same figure. This area was formed as a region with other conductive filaments. The conductive filaments first vaporize into single layers and then leave pores on the sample surface, as demonstrated in Figure 6i. The overall mechanism of the SET and RESET processes is shown in Figure 6j.

CONCLUSION

In summary, we have demonstrated a clear relationship between the resistance state and surface morphology. With the help of the FIB etching technique, a 3D model of the conductive filament was constructed. The model of the mechanism of the SET and RESET processes was improved based on our findings. First, multiple filaments with branches were formed just above the SET threshold and then simultaneously ruptured by Joule heating. As a result, the current in the SET process fluctuated until a thick filament was formed. With increasing current, the filament started to vaporize. The vapour coming from it exfoliated the single layers and left defects on them, including particles and pores.

Based on the SEM images, the formation of conductive filaments could be destructive for memristive devices. Therefore, adequate Joule heat was needed to assist the dissolution of the conductive filament into the electrolyte layer. However, excessive Joule heat was unavoidable during the DC sweep. For that reason, we performed a simulation of the electrical field and temperature gradient. The results showed the important role of the formed tungsten oxide layer, which caused a concentration of Joule heat near the bottom electrode. Therefore, two solutions, decreasing the compliance current and using tungsten as the top electrode, were tested in our experiments to decrease the Joule heat and improve the endurance of the device.

The FIB method is an effective way to probe the morphology of conductive filaments. It also offers an image of the conductive filament from the top or side view and is simple and powerful. Our experiments involving the 3D construction of conductive filaments exhibited unlimited potential for future applications.

AUTHOR INFORMATION

ACKNOWLEDGMENT

The author thanks Daniela Uhlirova for her fruitful suggestion in English proofreading. The author also thanks for financial support from the grant of the Ministry of Education, Youth- and Sports of Czech Republic (grant LM2023037), the European Regional Development Fund

Project, the project NANOMAT CZ.02.1.01/0.0/0.0/17_048/0007376 and the project of Faculty of Chemical Technology, University of Pardubice “Excellent teams” 2023， the grant of Hebei Normal University (L2021B12) and the HeBei NSF (QN2023054).

CONFLICT OF INTEREST

We declare that we have no conflict of interest.

REFERENCES

[1] H. Kim, D. Woo, S. Jin, H. Kwon, K. Kwon, D. Kim, D. Park, D. Kim, H. Jin, H. Choi, T. Shim, J. Park, Super-Linear-Threshold-Switching Selector with Multiple Jar-Shaped Cu-Filaments in the Amorphous Ge $_3$ Se $_7$ Resistive Switching Layer in a Cross-Point Synaptic Memristor Array, Advanced Materials 34 (2022) 2203643. https://doi.org/10.1002/adma.202203643.

[2] C. Schindler, M. Meier, R. Waser, M.N. Kozicki, Resistive switching in Ag-Ge-Se with extremely low write currents, in: 2007 Non-Volatile Memory Technology Symposium, IEEE, 2007: pp. 82–85. https://doi.org/10.1109/NVMT.2007.4389953.

[3] S. Bera, A.K. Katiyar, A.K. Sinha, S.P. Mondal, S.K. Ray, Resistive switching characteristics of a single Zn-doped CuS nanoball anchored with multi-walled carbon nanotubes, Mater Des 101 (2016) 197–203. https://doi.org/10.1016/j.matdes.2016.03.160.

[4] S. Hollmer, N. Gilbert, J. Dinh, D. Lewis, N. Derhacobian, A High Performance and Low Power Logic CMOS Compatible Embedded 1Mb CBRAM Non-Volatile Macro, in: 2011 3rd IEEE International Memory Workshop (IMW), IEEE, 2011: pp. 1–4. https://doi.org/10.1109/IMW.2011.5873221.

[5] A. Gubicza, D.Zs. Manrique, L. Pósa, C.J. Lambert, G. Mihály, M. Csontos, A. Halbritter, Asymmetry-induced resistive switching in Ag-Ag2S-Ag memristors enabling a simplified atomic-scale memory design, Sci Rep 6 (2016) 30775. https://doi.org/10.1038/srep30775.

[6] Y.T. Li, S.B. Long, H.B. Lü, Q. Liu, Q. Wang, Y. Wang, S. Zhang, W.T. Lian, S. Liu, M. Liu, Investigation of resistive switching behaviours in WO3-based RRAM devices, Chinese Physics B 20 (2011). https://doi.org/10.1088/1674-1056/20/1/017305.

[7] C. Schindler, S. Chandran Puthen Thermadam, R. Waser, M. N. Kozicki, Bipolar and Unipolar Resistive Switching in Cu-Doped SiO2, IEEE T-ED 54 (2007) 2762–2768. https://doi.org/10.1109/TED.2007.904402.

[8] I. Moriguchi, Y. Tsujigo, Y. Teraoka, S. Kagawa, Two-Dimensional Sol-Gel Synthesis of Hetero-Layered Nanostructure Composed of Ultrathin TiO2 and ZrO2 Laminae, Advanced Materials 11 (1999) 997–1000. https://doi.org/10.1002/(SICI)1521-4095(199908)11:12<997::AID-ADMA997>3.0.CO;2-L.

[9] T. Sakamoto, K. Lister, N. Banno, T. Hasegawa, K. Terabe, M. Aono, Electronic transport in Ta2O5 resistive switch, Appl Phys Lett 91 (2007) 092110-092110–3. https://doi.org/doi:10.1063/1.2777170.

[10] F.M. Simanjuntak, D. Panda, K.-H. Wei, T.-Y. Tseng, Status and Prospects of ZnO-Based Resistive Switching Memory Devices, Nanoscale Res Lett 11 (2016) 368. https://doi.org/10.1186/s11671-016-1570-y.

[11] J. Kolar, J.M. Macak, K. Terabe, T. Wagner, Down-scaling of resistive switching to nanoscale using porous anodic alumina membranes, J Mater Chem C Mater 2 (2014) 349. https://doi.org/10.1039/c3tc31969e.

[12] K. Terabe, T. Hasegawa, T. Nakayama, M. Aono, Quantized conductance atomic switch., Nature 433 (2005) 47–50. https://doi.org/10.1038/nature03190.

[13] M. Lanza, A. Sebastian, W.D. Lu, M. Le Gallo, M.-F. Chang, D. Akinwande, F.M. Puglisi, H.N. Alshareef, M. Liu, J.B. Roldan, Memristive technologies for data storage, computation, encryption, and radio-frequency communication, Science (1979) 376 (2022). https://doi.org/10.1126/science.abj9979.

[14] K. Cho, S.-J. Lee, K. Eshraghian, Memristor-CMOS logic and digital computational components, Microelectronics J 46 (2015) 214–220. https://doi.org/10.1016/j.mejo.2014.12.006.

[15] D.B. Strukov, K.K. Likharev, CMOL FPGA: a reconfigurable architecture for hybrid digital circuits with two-terminal nanodevices, Nanotechnology 16 (2005) 888–900. https://doi.org/10.1088/0957-4484/16/6/045.

[16] N. Ilyas, C. Li, J. Wang, X. Jiang, H. Fu, F. Liu, D. Gu, Y. Jiang, W. Li, A Modified SiO_2-Based Memristor with Reliable Switching and Multifunctional Synaptic Behaviors, J Phys Chem Lett 13 (2022) 884–893. https://doi.org/10.1021/acs.jpclett.1c03912.

[17] R. Waser, R. Dittmann, C. Staikov, K. Szot, Redox-based resistive switching memories nanoionic mechanisms, prospects, and challenges, Advanced Materials 21 (2009) 2632–2663. https://doi.org/10.1002/adma.200900375.

[18] R. Prakash, B.P. Singh Rathore, D. Kaur, Effect of top electrode material on resistive switching properties of WN based thin films for non volatile memory application, J Alloys Compd 726 (2017) 693–697. https://doi.org/10.1016/j.jallcom.2017.07.184.

[19] X. Guo, C. Schindler, S. Menzel, R. Waser, Understanding the switching-off mechanism in Ag+ migration based resistively switching model systems, Appl Phys Lett 91 (2007) 133513. https://doi.org/10.1063/1.2793686.

[20] T. Fujii, M. Arita, Y. Takahashi, I. Fujiwara, In situ transmission electron microscopy analysis of conductive filament during solid electrolyte resistance switching, Appl Phys Lett 98 (2011). https://doi.org/10.1063/1.3593494.

[21] C. Sang Jun, P. Gyeong Su, K. Ki Hong, C. Soohaeng, In Situ Observation of Voltage-Induced Multilevel Resistive Switching in Solid Electrolyte Memory, Advanced Materials 23 (2011) 3272–3277.

[22] C. Chang, J. Chen, C. Huang, C. Chiu, T. Lin, P. Yeh, W. Wu, Direct Observation of Dual-Filament Switching Behaviors in Ta_2O_5-Based Memristors, Small 13 (2017) 1603116. https://doi.org/10.1002/smll.201603116.

[23] B. Zhang, M. Fraenkl, J.M. Macak, T. Wagner, Ag filament and surface particle formation in Ag doped AsS2 thin film, Mater Lett 163 (2016) 4–7. https://doi.org/doi:10.1016/j.matlet.2015.08.131.

[24] T. Wei, Y. Lu, F. Zhang, J. Tang, B. Gao, P. Yu, H. Qian, H. Wu, Three-Dimensional Reconstruction of Conductive Filaments in HfO_x-Based Memristor, Advanced Materials 35 (2023). https://doi.org/10.1002/adma.202209925.

[25] Y. Zhang, C. Wang, X. Wu, Review of electrical stimulus methods of *in situ* transmission electron microscope to study resistive random access memory, Nanoscale 14 (2022) 9542–9552. https://doi.org/10.1039/D2NR01872A.

[26] D.M. Knotter, Etching Mechanism of Vitreous Silicon Dioxide in HF-Based Solutions, J Am Chem Soc 122 (2000) 4345–4351. https://doi.org/10.1021/ja993803z.

[27] Zhang， Bo, Cicmancova，Veronika, Ludvik，Benes, Slang，Stanislav, The structural modulation of amorphous 2D tungsten oxide materials in magnetron sputtering, Adv Mater Interfaces (2022).

[28] C.-J. Wang, S. Jou, Study of copper-doped SiO2 films prepared by co-sputtering of copper and SiO2, Journal of Physics and Chemistry of Solids 69 (2008) 523–526. https://doi.org/10.1016/j.jpcs.2007.07.035.

[29] Y. Yang, Y. Takahashi, A. Tsurumaki-Fukuchi, M. Arita, M. Moors, M. Buckwell, A. Mehonic, A.J. Kenyon, Probing electrochemistry at the nanoscale: in situ TEM and STM characterizations of conducting filaments in memristive devices, J Electroceram 39 (2017) 73–93. https://doi.org/10.1007/s10832-017-0069-y.

[30] S. Gao, C. Chen, Z. Zhai, H.Y. Liu, Y.S. Lin, S.Z. Li, S.H. Lu, G.Y. Wang, C. Song, F. Zeng, F. Pan, Resistive switching and conductance quantization in Ag/SiO2/indium tin oxide resistive memories, Appl Phys Lett 105 (2014). https://doi.org/10.1063/1.4893277.

[31] A. Mehonic, A. Vrajitoarea, S. Cueff, S. Hudziak, H. Howe, C. Labbé, R. Rizk, M. Pepper, A.J. Kenyon, Quantum Conductance in Silicon Oxide Resistive Memory Devices, Sci Rep 3 (2013) 2708. https://doi.org/10.1038/srep02708.

[32] M. Lübben, S. Menzel, S.G. Park, M. Yang, R. Waser, I. Valov, SET kinetics of electrochemical metallization cells: influence of counter-electrodes in SiO_2 /Ag based systems, Nanotechnology 28 (2017) 135205. https://doi.org/10.1088/1361-6528/aa5e59.

[33] S. Tappertzhofen, R. Ahlmann, Anodic oxidation effects at the copper/silicon oxide interface, Memories - Materials, Devices, Circuits and Systems 1 (2022) 100004. https://doi.org/10.1016/j.memori.2022.100004.

[34] M. Lübben, S. Wiefels, R. Waser, I. Valov, Processes and Effects of Oxygen and Moisture in Resistively Switching TaO_x and HfO_x , Adv Electron Mater 4 (2018). https://doi.org/10.1002/aelm.201700458.

[35] T. Wagner, J. Gutwirth, P. Nemec, M. Frumar, M. Vlcek, V. Perina, A. Mackova, V. Hnatovitz, Amorphous chalcogenide AgSbS2 films prepared by pulsed laser deposition, Appl Phys A Mater Sci Process 79 (2004) 1561–1562. http://www.scopus.com/inward/record.url?eid=2-s2.0-4344627248&partnerID=40&md5=93de010a35bebb9b598eb33e4b7429b2.

[36] M. Lanza, R. Waser, D. Ielmini, J.J. Yang, L. Goux, J. Suñe, A.J. Kenyon, A. Mehonic, S. Spiga, V. Rana, S. Wiefels, S. Menzel, I. Valov, M.A. Villena, E. Miranda, X. Jing, F. Campabadal, M.B. Gonzalez, F. Aguirre, F. Palumbo, K. Zhu, J.B. Roldan, F.M. Puglisi, L. Larcher, T.-H. Hou, T. Prodromakis, Y. Yang, P. Huang, T. Wan, Y. Chai, K.L. Pey, N. Raghavan, S. Dueñas, T. Wang, Q. Xia, S. Pazos, Standards for the Characterization of Endurance in Resistive Switching Devices, ACS Nano 15 (2021) 17214–17231. https://doi.org/10.1021/acsnano.1c06980.

[37] R. Mahapatra, S. Maji, A.B. Horsfall, N.G. Wright, Temperature impact on switching characteristics of resistive memory devices with HfOx/TiOx/HfOx stack dielectric, Microelectron Eng 138 (2015) 118–121. https://doi.org/10.1016/j.mee.2015.03.008.

[38] J. Joshua Yang, F. Miao, M.D. Pickett, D.A. Ohlberg, D.R. Stewart, C.N. Lau, R.S. Williams, The mechanism of electroforming of metal oxide memristive switches., Nanotechnology 20 (2009) 215201. https://doi.org/10.1088/0957-4484/21/33/339803.

[39] Y. Chao Yang, F. Pan, F. Zeng, Bipolar resistance switching in high-performance Cu/ZnO:Mn/Pt nonvolatile memories: active region and influence of Joule heating, New J Phys 12 (2010) 023008. https://doi.org/10.1088/1367-2630/12/2/023008.